



A (non-)hydrostatic free-surface numerical model for two-layer flows



Jan Bohacek^{a,*}, Abdellah Kharicha^b, Andreas Ludwig^a, Menghuai Wu^b,
Ebrahim Karimi-Sibaki^b, Armin Paar^c, Michael Brandner^c, Leonel Elizondo^c,
Thomas Trickl^c

^a Department of Metallurgy, Montanuniversitaet Leoben, Franz-Joseph Strasse 18, 8700 Leoben, Austria

^b Christian Doppler Lab for Advanced Simulation of Solidification and Melting, Dept. of Metallurgy, Montanuniversitaet Leoben, Franz-Joseph Strasse 18, 8700 Leoben, Austria

^c Eisenwerk Sulzau-Werfen, R.&E. Weinberger AG, A-5441 Tenneck, Austria

ARTICLE INFO

Article history:

Available online 18 April 2017

Keywords:

numerical modeling
free-surface model
centrifugal casting
solidification
advection-diffusion equation
shallow water equations

ABSTRACT

A semi-implicit (non-)hydrostatic free-surface numerical model for two layer flows is derived from the Navier–Stokes equations by applying kinematic boundary conditions at moving interfaces and by decomposing the pressure into the hydrostatic and the hydrodynamic part. When the latter is ignored, the algorithm conveniently transforms into a solver for a hydrostatic flow. In addition, when the vertical grid spacing is larger than the layer depths, the algorithm naturally degenerates into a solver for the shallow water equations. In this paper, the presented numerical model is developed for the horizontal centrifugal casting, a metallurgical process, in which a liquid metal is poured into a horizontally rotating cylindrical mold. The centrifugal force pushes the liquid metal toward the mold wall resulting in a formation of a sleeve with a uniform thickness. The mold gradually extracts the sensible and the latent heat from the sleeve, which eventually becomes solid. Often a second layer of another material is introduced during the solidification of the first layer. The proposed free-surface model is therefore coupled with the heat advection-diffusion equation with a stiff latent heat source term representing the solidification. The numerical results show a good agreement with measurements of temperatures performed in the plant. A validation of the proposed model is also provided with the help of using other numerical techniques such as the approximate Riemann solver for the two layer shallow water equations and the volume of fluid method.

© 2017 Elsevier Inc. All rights reserved.

1. Introduction

Quite a few numerical models have been derived from the Navier–Stokes (N–S) equations to study free-surface flows. The main task of these models is to account for the interface separating fluid domains and being generally in motion. A typical fluid flow problem may involve one, two or more immiscible fluids. No matter the numerical method used, calculation steps can be summarized as: (a) set the boundary conditions at the interface; (b) advance the interface in time; (c) identify the position of the interface. According to [1,2], the most common numerical methods in this field are

* Corresponding author.

E-mail address: bohacek.jan@gmail.com (J. Bohacek).

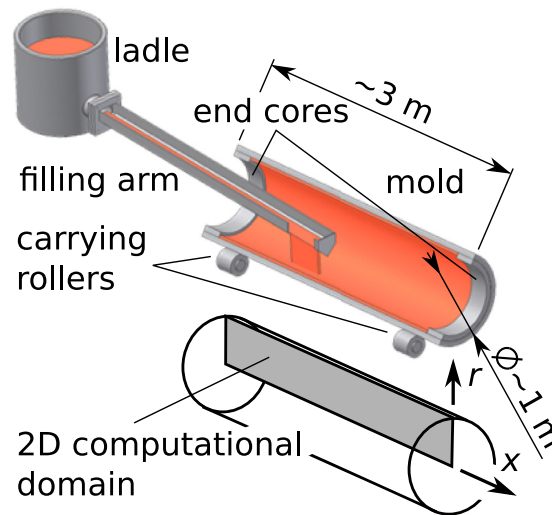


Fig. 1. A scheme of the horizontal centrifugal casting process with a computational domain and coordinates shown below it.

level-set [3,4], volume-of-fluid (VOF) [5], phase-field [6,7], particle method (marker-and-cell) [8], and the interface tracking [9]. Depending on the viewpoint of the observer—Eulerian or Lagrangian—interface capturing (VOF) and interface tracking approach can be distinguished respectively [10]. A main advantage of the earlier over the latter is that the topology of the interface is inherently treated, which allows for a description of much more complex interfaces. On the other hand, since the exact position of the interface is not exactly known, the treatment of boundary conditions, discontinuities across the interface and mass conservation still remain a challenge. For comparable grid sizes, interface tracking methods yield more accurate representation of the interface. Free-surface flows with less complicated interface topologies are generally solved by interface tracking methods, in which all grid points are treated either in a Lagrangian fashion or in an Arbitrary Lagrangian-Eulerian (ALE) approach [11], at which only the grid points close to the free-surface are being relocated. The ALE approach is advantageous when the liquid layer thickness goes to zero. In that case, the entire thickness of the layer is contained within a single cell along the vertical direction. Therefore, the 3D N-S equations collapse into the 2D shallow water equations (SWE) [12,13] due to the hydrostatic pressure assumption commonly applied within the interface cell.

In the present paper, a numerical model of horizontal centrifugal casting (HCC) process is introduced. In the HCC process [14–18], the liquid metal is poured inside a horizontal cylindrical mold rotating at high rates. Centrifugal forces push the liquid metal toward the wall of the mold with the radius R , resulting in a uniform thickness of the layer. The relatively cold mold extracts the heat from the liquid metal; therefore, solidification gradually proceeds toward the free-surface of the layer (Fig. 1). Often, when the liquid metal is partially solidified, an additional liquid of a different material is poured in. Most of the numerical studies solve the heat diffusion equation with a phase change source term. In order to account for the heat advection due to the flow, the thermal conductivity is artificially increased in the liquid region [19]. Several works in this area can be also found dedicated to the flow simulation, from which some of them rely on commercial CFD packages [20] and some on in-house codes, for example [21,22].

In the HCC, as a simple, nearly flat, free-surface and rather a weak effect of the surrounding air on dynamics of the liquid layer can be anticipated, an interface tracking approach is adopted here, inspired by Casulli [23–25] and further extended to account for two immiscible liquid layers. A robust finite difference-finite volume algorithm is derived from the non-hydrostatic N-S equations and it is suitable for structured and also unstructured grids provided the orthogonal layering of elements in the radial direction (Fig. 2). Due to the geometry configuration of the HCC, the cylindrical coordinates are used. Therefore, the axial, radial, and tangential axis notation can be seen throughout this paper. The pressure term is conveniently decomposed into the hydrostatic and the hydrodynamic part, which makes the algorithm very efficient especially when dealing with hydrostatic or nearly hydrostatic flows. The convective term and the axial viscous term are discretized explicitly using the reconstruction of the Lagrangian trajectory, especially popular in atmosphere modeling [26,27]. The resulting algorithm is mass conservative. In addition, when only a single layer of volume elements is considered, the algorithm degenerates into the shallow water equations. The proposed formulation can inherently handle drying and flooding of dry surfaces. In a subsequent step, the flow algorithm is followed by a stable finite volume scheme for the heat advection-diffusion equation with the solidification source term. Consequently, temperature differences result in thermal convection, which is in the N-S equations realized through a baroclinic pressure term.

In the next sections, the governing equations are firstly introduced, followed by detailed steps of the algorithm. Finally, results are presented in the form of numerical examples, some of them verified against temperature measurements from the plant and some against other numerical techniques.

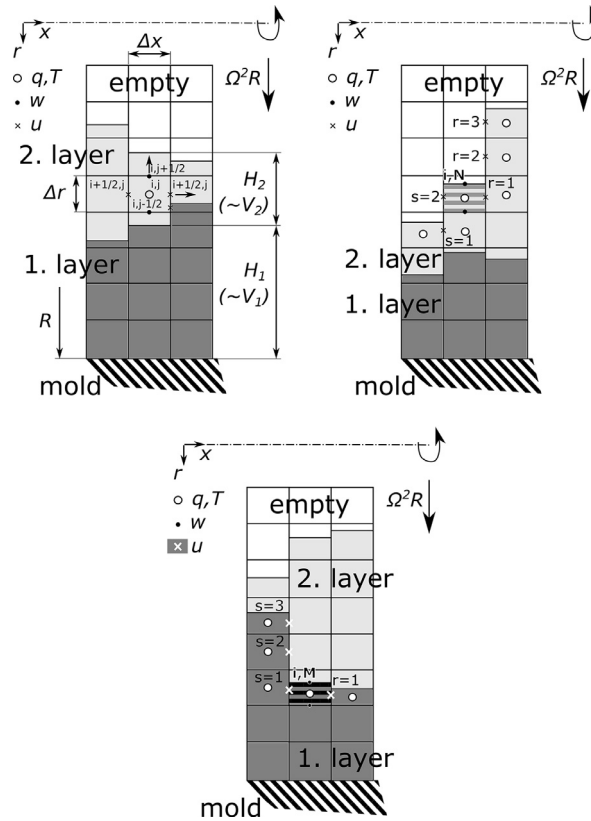


Fig. 2. Two-dimensional structured orthogonal staggered grid; (a) fluctuations of the free-surface/the interface confined within a single layer of cells in the radial direction; (b) the free-surface surpassing more than one layer of cells; (c) the interface surpassing more than one layer of cells.

2. Governing equations

For the sake of clarity, not losing generality, the algorithm is presented in a two-dimensional axisymmetric form, for the axial and the radial coordinate, x and r , respectively. (The size of the tangential sector is 1 rad.) Conservation of mass, momentum, and energy are governed by transport equations. Starting with the momentum equations, due to the high rotation rate Ω they are written in the rotating frame i.e. fictitious forces must be accounted for. In the cylindrical coordinates the momentum equations can be written as:

$$\frac{\partial u}{\partial t} + u \frac{\partial u}{\partial x} + w \frac{\partial u}{\partial r} = -\frac{\partial p}{\partial x} + \nu \left[\frac{\partial^2 u}{\partial x^2} + \frac{1}{r} \frac{\partial}{\partial r} \left(r \frac{\partial u}{\partial r} \right) \right] - \frac{\nu}{K} u \quad (1)$$

$$\frac{\partial w}{\partial t} + u \frac{\partial w}{\partial x} + w \frac{\partial w}{\partial r} = -\frac{\partial p}{\partial r} + \frac{\rho}{\rho_0} \Omega^2 r + \nu \left[\frac{\partial^2 w}{\partial x^2} + \frac{1}{r} \frac{\partial}{\partial r} \left(r \frac{\partial w}{\partial r} \right) - \frac{w}{r^2} \right] - \frac{\nu}{K} w, \quad (2)$$

where u and w are the axial and radial components of velocity and p the normalized pressure respectively. The kinematic viscosity and the density, which may depend on temperature $T(\rho = \rho(T))$, are denoted by Greek symbols ν and ρ . The permeability, K , is a part of the momentum sink due to the drag of solidifying dendrites and is defined as a function of the primary dendrite arm spacing and the liquid fraction, g_l [28,29]. Such momentum sink is only active in the solidifying region. The normalized pressure p is defined as a ratio between the pressure and a constant reference density ρ_0 . The tangential component of the Coriolis acceleration is the only one different from zero. As the tangential dimension is omitted in this study, the Coriolis term does not appear in (1)-(2). Compared to the centrifugal force, expressed by the second term on the rhs of (2), the force of gravity is small and can be thus neglected. In fact, it cannot be present in (2) due to the rotating frame used and the two-dimensional (x, r) case. The mass conservation obeys the incompressibility condition, given by:

$$\frac{\partial u}{\partial x} + \frac{1}{r} \frac{\partial (rw)}{\partial r} = 0 \quad (3)$$

In addition, the energy transport equation represented by the heat advection–diffusion equation takes the following form:

$$\rho c_p \left(\frac{\partial T}{\partial t} + u \frac{\partial T}{\partial x} + w \frac{\partial T}{\partial r} \right) = \frac{\partial}{\partial x} \left(k \frac{\partial T}{\partial x} \right) + \frac{1}{r} \frac{\partial}{\partial r} \left(rk \frac{\partial T}{\partial r} \right) - \rho L_f \frac{\partial g_l}{\partial t} \tag{4}$$

where c_p , k , and L_f are the specific heat, the thermal conductivity, and the latent heat respectively. In order to describe deformations of the free-surface and the interface between the outer and the inner layer (in the following text referred to as the interface) combining kinematic boundary conditions and the continuity Eq. (3) integrated over the depth of each layer gives a set of free-surface equations, written as:

$$\frac{\partial V_1}{\partial t} + \sum_R^{R-H_1} ur dr = 0 \tag{5}$$

$$\frac{\partial V_2}{\partial t} + \sum_{R-H_1}^{R-H_1-H_2} ur dr = 0, \tag{6}$$

where H and V are the local depth of the layer and its corresponding volume calculated for the element size dx . The indices $[\dots]_{1,2}$ signify the outer and the inner layer respectively.

In (1)-(2), the pressure p is decomposed into the sum of the hydrostatic and the hydrodynamic part q . Unlike the hydrostatic pressure induced by the gravitational acceleration, its centrifugal counterpart is a nonlinear function of radial position r . If the depths $H_{1,2}$ are $\ll R$, it is advisable to replace the centrifugal term $\Omega^2 r$ with $\Omega^2 R$, where R is the radius of the cylindrical wall (Fig. 2). This strategy is also convenient in order to avoid lengthy formulas and thus maintain readability of the present text. Then, the pressure $p_{1,2}$ scaled by the reference density of each layer $\rho_{01,02}$ takes the following form:

$$p_1 = \Omega^2 R \left(r - R + H_1 + \frac{\rho_{02}}{\rho_{01}} H_2 \right) + \Omega^2 R \sum_{R-H_1}^{R-H_1-H_2} \frac{\rho_{01} - \rho_1}{\rho_{01}} dr + \Omega^2 R \sum_r^{R-H_1} \frac{\rho_{01} - \rho_1}{\rho_{01}} dr + q \tag{7}$$

$$p_2 = \Omega^2 R (r - R + H_1 + H_2) + \Omega^2 R \sum_r^{R-H_1-H_2} \frac{\rho_{02} - \rho_2}{\rho_{02}} dr + q. \tag{8}$$

Due to the variable density $\rho(T)$, it is common to further split the hydrostatic pressure into the barotropic component, represented by the first terms of (7)-(8), and the baroclinic component, represented by the terms with integrals. The atmospheric pressure is set to zero, thus not appearing in (7)-(8). Eqs. (7)-(8) are substituted into (1)-(2) for each layer separately. Note that the gradient of the hydrostatic pressure cancels out with the centrifugal term $\rho/\rho_0 \Omega^2 R$ in (2); therefore, only the hydrodynamic part q remains.

3. Numerical algorithm

The spatial discretization of the physical domain is realized by dividing it into $N_x N_r$ orthogonal structured cells with a axial and radial size, Δx and Δr . Unlike Δx being fixed, the radial size Δr is only constant in the bulk, equal to the difference between the outer and the inner level surface (Fig. 2). At the free-surface and the interface it is calculated as a difference between the outer level surface and the free-surface or the interface respectively. Cell centers are consecutively numbered with indices i, j . The field variables are stored in a staggered manner. While the velocities are defined at the cell faces using half indices, other scalar fields such as the hydrodynamic pressure q , the temperature T , and the liquid fraction g_l are located at the cell centers. Finally, the depth and the volume of each layer are indexed along the axial coordinate as H_i and V_i respectively.

Here, a semi-implicit Eulerian–Lagrangian fractional step scheme is adopted in order to arrive at stable and efficient numerical algorithm. The pressure is discretized by the θ -method [30]. In a predictor step, the preliminary velocity field and positions of the free-surface and the interface are calculated by neglecting the implicit contribution of the hydrodynamic pressure q . Secondly, the Poisson’s equation is solved for the pressure q in a corrector step, which is finally used to correct the preliminary quantities obtained in the predictor step. The resulting velocity field is mass conservative.

3.1. Predictor step

By discretizing (1) e.g. for the inner layer (2) using a semi-implicit finite-difference scheme, the axial velocity component u at radial faces $i + 1/2, j$ yields the following form:

$$\begin{aligned} \tilde{u}_{i+1/2,j}^{n+1} = & F u_{i+1/2,j}^n - \theta \frac{\Delta t}{\Delta x} \left(\Omega^2 R (H_{1,i+1}^{n+1} - H_{1,i}^{n+1} + H_{2,i}^{n+1} - H_{2,i}^{n+1}) \right) - \Delta t \frac{v}{K} \tilde{u}_{i+1/2,j}^{n+1} \\ & + v \frac{\Delta t}{\Delta r_{i+1/2,j}^n} \frac{1}{r_{i+1/2,j}^n} \left(r_{i+1/2,j+1/2}^n \frac{\tilde{u}_{i+1/2,j+1}^{n+1} - \tilde{u}_{i+1/2,j}^{n+1}}{\Delta r_{i+1/2,j+1/2}^n} - r_{i+1/2,j-1/2}^n \frac{\tilde{u}_{i+1/2,j}^{n+1} - \tilde{u}_{i+1/2,j-1}^{n+1}}{\Delta r_{i+1/2,j-1/2}^n} \right) \end{aligned} \tag{9}$$

Discretization of (1) for the outer layer (1) is an analogy. The tilde symbol denotes a preliminary unknown calculated in the predictor step going to be later updated in the corrector step. The current and the old time step are denoted by $n + 1$ and n superscripts. The implicit factor θ is used to split both, the barotropic and the hydrodynamic pressure, into an implicit and an explicit contribution scaled by θ and $(1 - \theta)$ respectively. The implicit factor θ has to be chosen in the range $1/2 \leq \theta \leq 1$. In the predictor step, only the barotropic part of the pressure p_2 (8) is treated implicitly multiplied by the implicit factor θ and appears as a second term on the rhs of (9). The implicit hydrodynamic part q of the pressure p_2 is considered separately in the corrector step. The explicit part of the barotropic and the hydrodynamic pressure multiplied by $(1 - \theta)$ is hidden in the term $Fu_{i+1/2,j}^n$, see the third term on the rhs of (11). The baroclinic pressure, the term with an integral in (8), is handled fully explicitly and is also hidden in the term $Fu_{i+1/2,j}^n$, see the last term on the rhs of (11). In addition, since the layer depths are significantly smaller than the axial scale, axial viscosity terms are treated explicitly and also enter the term $Fu_{i+1/2,j}^n$. Finally, the lhs of (1) is discretized by reconstructing the Lagrangian trajectory. The total derivative of the axial velocity component u can be written as the following:

$$\frac{du}{dt} = \frac{\tilde{u}_{i+1/2,j}^{n+1} - u_{i+1/2,j}^*}{\Delta t}, \tag{10}$$

where $u_{i+1/2,j}^*$ is the interpolated axial velocity component recorded at time t_n at the end of the Lagrangian trajectory and again goes inside the term $Fu_{i+1/2,j}^n$ and can be expressed as

$$\begin{aligned} Fu_{i+1/2,j}^n &= u_{i+1/2,j}^* + \Delta t v \frac{u_{i+3/2,j}^* - 2u_{i+1/2,j}^* + u_{i-1/2,j}^*}{\Delta x^2} \\ &\quad - (1 - \theta)\Omega^2 R \frac{\Delta t}{\Delta x} (\Omega^2 R (H_{1,i+1}^n - H_{1,i}^n + H_{2,i}^n - H_{2,i}^n) + q_{i+1,j}^n - q_{i,j}^n) \\ &\quad - \Omega^2 R \frac{\Delta t}{\Delta x} \left(\sum_{r_{i+1,j}^n}^{R-H_{1,i+1}^n-H_{2,i+1}^n} \frac{\rho_{02} - \rho_{2,i+1,j}^n}{\rho_{02}} dr - \sum_{r_{i,j}^n}^{R-H_{1,i}^n-H_{2,i}^n} \frac{\rho_{02} - \rho_{2,i,j}^n}{\rho_{02}} dr \right) \end{aligned} \tag{11}$$

Similarly to (1), (2) can be discretized as

$$\begin{aligned} \tilde{w}_{i,j+1/2}^{n+1} &= Fw_{i,j+1/2}^n - \Delta t \frac{v}{K} \tilde{w}_{i,j+1/2}^{n+1} \\ &\quad + v \frac{\Delta t}{\Delta r_{i,j+1/2}^n} \frac{1}{r_{i,j+1/2}^n} \left(r_{i,j+1}^{n+1} \frac{\tilde{w}_{i,j+3/2}^{n+1} - \tilde{w}_{i,j+1/2}^{n+1}}{\Delta r_{i,j+1}^{n+1}} - r_{i,j}^{n+1} \frac{\tilde{w}_{i,j+1/2}^{n+1} - \tilde{w}_{i,j-1/2}^{n+1}}{\Delta r_{i,j}^{n+1}} \right) - v \Delta t \frac{\tilde{w}_{i,j+1/2}^{n+1}}{r_{i,j+1/2}^{2,n}} \end{aligned} \tag{12}$$

where $Fw_{i,j+1/2}^n$ is again the finite difference operator similar to that in (9). It comprises axial viscous terms, the interpolated radial velocity component $w_{i,j+1/2}^*$, and the explicit contribution of the hydrodynamic pressure q . In the predictor step, since the implicit contribution of the hydrodynamic pressure is neglected, the momentum equations (9) and (12) are independent of each other and can be therefore solved separately. Eq. (12) forms a symmetric tridiagonal system, which can be easily solved by preconditioned conjugate gradient method [31]. Unlike (12), Eq. (9) cannot be readily solved, as it is coupled to the unknown layer depths $H_{1,2,i}^{n+1}$. In order to determine $\tilde{H}_{1,2,i}^{n+1}$, the preliminary field of the axial velocity component $\tilde{u}_{i+1/2,j}^{n+1}$ must satisfy discrete versions of free-surface equations (5)-(6) for each layer.

$$\begin{aligned} \tilde{V}_{1,i}^{n+1} &= V_{1,i}^n - \theta \Delta t \left(\sum_{j=1}^M r_{i+1/2,j}^n \Delta r_{i+1/2,j}^n \tilde{u}_{i+1/2,j}^{n+1} - \sum_{j=1}^M r_{i-1/2,j}^n \Delta r_{i-1/2,j}^n \tilde{u}_{i-1/2,j}^{n+1} \right) \\ &\quad - (1 - \theta) \Delta t \left(\sum_{j=1}^M r_{i+1/2,j}^n \Delta r_{i+1/2,j}^n u_{i+1/2,j}^n - \sum_{j=1}^M r_{i-1/2,j}^n \Delta r_{i-1/2,j}^n u_{i-1/2,j}^n \right) \end{aligned} \tag{13}$$

$$\begin{aligned} \tilde{V}_{2,i}^{n+1} &= V_{2,i}^n - \theta \Delta t \left(\sum_{j=M+1}^N r_{i+1/2,j}^n \Delta r_{i+1/2,j}^n \tilde{u}_{i+1/2,j}^{n+1} - \sum_{j=M+1}^N r_{i-1/2,j}^n \Delta r_{i-1/2,j}^n \tilde{u}_{i-1/2,j}^{n+1} \right) \\ &\quad - (1 - \theta) \Delta t \left(\sum_{j=M+1}^N r_{i+1/2,j}^n \Delta r_{i+1/2,j}^n u_{i+1/2,j}^n - \sum_{j=M+1}^N r_{i-1/2,j}^n \Delta r_{i-1/2,j}^n u_{i-1/2,j}^n \right) \end{aligned} \tag{14}$$

where M and N , $1 \leq M \leq N \leq N_r$, may vary both in time and space and denote the radial index j of the interface cell and the free-surface respectively. After multiplying the momentum equation (9) by $\Delta r_{i+1/2,j}^n$ and substituting for the pressure p from (7)-(8) for the outer (1) and the inner layer (2) respectively, we will arrive at the set of linear equations, which written in matrix notation take the following form

$$\mathbf{A}_{i+1/2}^n \tilde{\mathbf{U}}_{i+1/2}^{n+1} = \mathbf{C}_{i+1/2}^n - \Omega^2 R \frac{\Delta t}{\Delta x} (\tilde{H}_{1,i+1}^{n+1} - \tilde{H}_{1,i}^{n+1}) \mathbf{\Delta R}_{i+1/2}^n - \Omega^2 R \frac{\Delta t}{\Delta x} (\tilde{H}_{2,i+1}^{n+1} - \tilde{H}_{2,i}^{n+1}) \mathbf{\Theta}_{i+1/2}^n * \mathbf{\Delta R}_{i+1/2}^n \tag{15}$$

where $\tilde{\mathbf{U}}_{i+1/2}^{n+1}$, $\mathbf{G}_{i+1/2}^n$, $\Delta \mathbf{R}_{i+1/2}^n$, $\Theta_{i+1/2}^n$ are column vectors and $\mathbf{A}_{i+1/2}^n$ is a tridiagonal coefficient matrix. Explicit terms are contained in $\mathbf{G}_{i+1/2}^n$. Implicit terms are reflected in $\mathbf{A}_{i+1/2}^n$. In each layer, barotropic parts of the hydrostatic pressure (7)-(8), namely the terms with \tilde{H}_2 , differ only by the scale of density ratio ρ_{02}/ρ_{01} , which is included in the column vector $\Theta_{i+1/2}^n$. The operator [*] signifies a piecewise-element multiplication. Omitting the subscripts and the superscripts, the vectors $\tilde{\mathbf{U}}, \Delta \mathbf{R}, \Theta$ are defined as the following:

$$\tilde{\mathbf{U}} = \begin{bmatrix} \tilde{u}_1 \\ \vdots \\ \tilde{u}_M \\ \tilde{u}_{M+1} \\ \vdots \\ \tilde{u}_N \end{bmatrix}, \quad \Delta \mathbf{R} = \Delta \mathbf{R}_1 + \Delta \mathbf{R}_2 = \begin{bmatrix} \Delta r_1 \\ \vdots \\ \Delta r_M \\ 0 \\ \vdots \\ 0 \end{bmatrix} + \begin{bmatrix} 0 \\ \vdots \\ 0 \\ \Delta r_{M+1} \\ \vdots \\ \Delta r_N \end{bmatrix},$$

$$\Theta = \begin{bmatrix} \rho_{02}/\rho_{01} \\ \vdots \\ \rho_{02}/\rho_{01} \\ 1 \\ \vdots \\ 1 \end{bmatrix}. \tag{16}$$

Although it is straightforward to construct the coefficient matrix of implicit terms \mathbf{A} and the vector of explicit terms \mathbf{G} using (9), they are too long to be shown here. The coefficient \mathbf{A} matrix is a tridiagonal positive definite matrix. Note that the size of vectors $\tilde{\mathbf{U}}, \mathbf{G}, \Delta \mathbf{R}, \Theta$ and the matrix \mathbf{A} may vary or even disappear depending on actual layer depths $H_{1,2}$.

Similarly to (9), (13) and (14) can also be written using vector notation as

$$\tilde{V}_{1,i}^{n+1} = V_{1,i}^n - \theta \Delta t \left((\mathbf{R}_{i+1/2}^n * \Delta \mathbf{R}_{1,i+1/2}^n)^T \tilde{\mathbf{U}}_{i+1/2}^{n+1} - (\mathbf{R}_{i-1/2}^n * \Delta \mathbf{R}_{1,i-1/2}^n)^T \tilde{\mathbf{U}}_{i-1/2}^{n+1} \right) - (1 - \theta) \Delta t \left((\mathbf{R}_{i+1/2}^n * \Delta \mathbf{R}_{1,i+1/2}^n)^T \mathbf{U}_{i+1/2}^n - (\mathbf{R}_{i-1/2}^n * \Delta \mathbf{R}_{1,i-1/2}^n)^T \mathbf{U}_{i-1/2}^n \right) \tag{17}$$

$$\tilde{V}_{2,i}^{n+1} = V_{2,i}^n - \theta \Delta t \left((\mathbf{R}_{i+1/2}^n * \Delta \mathbf{R}_{2,i+1/2}^n)^T \tilde{\mathbf{U}}_{i+1/2}^{n+1} - (\mathbf{R}_{i-1/2}^n * \Delta \mathbf{R}_{2,i-1/2}^n)^T \tilde{\mathbf{U}}_{i-1/2}^{n+1} \right) - (1 - \theta) \Delta t \left((\mathbf{R}_{i+1/2}^n * \Delta \mathbf{R}_{2,i+1/2}^n)^T \mathbf{U}_{i+1/2}^n - (\mathbf{R}_{i-1/2}^n * \Delta \mathbf{R}_{2,i-1/2}^n)^T \mathbf{U}_{i-1/2}^n \right) \tag{18}$$

Formal substitution for $\tilde{\mathbf{U}}_{i+1/2}^{n+1}$ from (15) into (17) and (18) yields

$$\tilde{V}_{1,i}^{n+1} = V_{1,i}^n - \theta \Omega^2 R \frac{\Delta t^2}{\Delta X} \left([(\mathbf{R} * \Delta \mathbf{R}_1)^T \mathbf{A}^{-1} \Delta \mathbf{R}]_{i+1/2}^n (\tilde{H}_{1,i+1}^{n+1} - \tilde{H}_{1,i}^{n+1}) - [(\mathbf{R} * \Delta \mathbf{R}_1)^T \mathbf{A}^{-1} \Delta \mathbf{R}]_{i-1/2}^n (\tilde{H}_{1,i}^{n+1} - \tilde{H}_{1,i-1}^{n+1}) \right) - \theta \Omega^2 R \frac{\Delta t^2}{\Delta X} \left([(\mathbf{R} * \Delta \mathbf{R}_1)^T \mathbf{A}^{-1} (\Theta * \Delta \mathbf{R})]_{i+1/2}^n (\tilde{H}_{2,i+1}^{n+1} - \tilde{H}_{2,i}^{n+1}) - [(\mathbf{R} * \Delta \mathbf{R}_1)^T \mathbf{A}^{-1} (\Theta * \Delta \mathbf{R})]_{i-1/2}^n (\tilde{H}_{2,i}^{n+1} - \tilde{H}_{2,i-1}^{n+1}) \right) - \theta \Delta t \left([(\mathbf{R} * \Delta \mathbf{R}_1)^T \mathbf{A}^{-1} \mathbf{G}]_{i+1/2}^n - [(\mathbf{R} * \Delta \mathbf{R}_1)^T \mathbf{A}^{-1} \mathbf{G}]_{i-1/2}^n \right) - (1 - \theta) \Delta t \left([(\mathbf{R} * \Delta \mathbf{R}_1)^T \mathbf{U}]_{i+1/2}^n - [(\mathbf{R} * \Delta \mathbf{R}_1)^T \mathbf{U}]_{i-1/2}^n \right) \tag{19}$$

$$\tilde{V}_{2,i}^{n+1} = V_{2,i}^n - \theta \Omega^2 R \frac{\Delta t^2}{\Delta X} \left([(\mathbf{R} * \Delta \mathbf{R}_2)^T \mathbf{A}^{-1} \Delta \mathbf{R}]_{i+1/2}^n (\tilde{H}_{1,i+1}^{n+1} - \tilde{H}_{1,i}^{n+1}) - [(\mathbf{R} * \Delta \mathbf{R}_2)^T \mathbf{A}^{-1} \Delta \mathbf{R}]_{i-1/2}^n (\tilde{H}_{1,i}^{n+1} - \tilde{H}_{1,i-1}^{n+1}) \right) - \theta \Omega^2 R \frac{\Delta t^2}{\Delta X} \left([(\mathbf{R} * \Delta \mathbf{R}_2)^T \mathbf{A}^{-1} (\Theta * \Delta \mathbf{R})]_{i+1/2}^n (\tilde{H}_{2,i+1}^{n+1} - \tilde{H}_{2,i}^{n+1}) - [(\mathbf{R} * \Delta \mathbf{R}_2)^T \mathbf{A}^{-1} (\Theta * \Delta \mathbf{R})]_{i-1/2}^n (\tilde{H}_{2,i}^{n+1} - \tilde{H}_{2,i-1}^{n+1}) \right) - \theta \Delta t \left([(\mathbf{R} * \Delta \mathbf{R}_2)^T \mathbf{A}^{-1} \mathbf{G}]_{i+1/2}^n - [(\mathbf{R} * \Delta \mathbf{R}_2)^T \mathbf{A}^{-1} \mathbf{G}]_{i-1/2}^n \right) - (1 - \theta) \Delta t \left([(\mathbf{R} * \Delta \mathbf{R}_2)^T \mathbf{U}]_{i+1/2}^n - [(\mathbf{R} * \Delta \mathbf{R}_2)^T \mathbf{U}]_{i-1/2}^n \right) \tag{20}$$

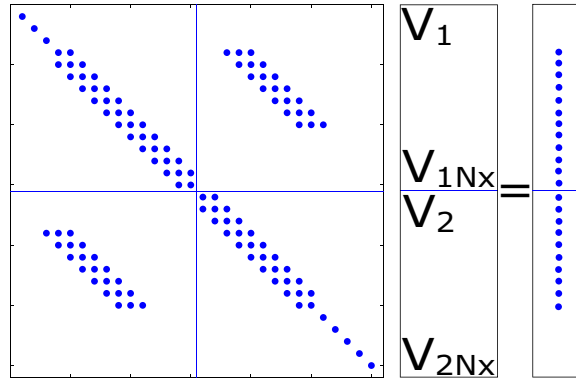


Fig. 3. A visualization of the system of coupled equations (19)-(20) for $\tilde{V}_{1,1}^{n+1}$ and $\tilde{V}_{1,1}^{n+1}$ with an illustrative demonstration of vanishing depth of each layer.

In order to allow us to solve (19) and (20) for $V_{1,2}$, the layer depths $H_{1,2}$ has to be firstly replaced by axisymmetric relations linking $H_{1,2}$ with $V_{1,2}$, which read

$$H_1 = R - \sqrt{R^2 - \frac{2V_1}{\Delta x}}, H_2 = R - H_1 - \sqrt{(R - H_1)^2 - \frac{2V_2}{\Delta x}} \tag{21}$$

As the formulas given by (21) are nonlinear, a linearization technique is applied and (21) become

$$H_1^{n+1} = H_1^n + H_1^n(V_1^{n+1} - V_1^n), H_2^{n+1} = H_2^n + H_2^n(V_2^{n+1} - V_2^n), \tag{22}$$

where H_1^n and H_2^n are $H_1^n = \frac{1}{\Delta x \sqrt{R^2 - \frac{2V_1^n}{\Delta x}}}$ and $H_2^n = \frac{1}{\Delta x \sqrt{(R - H_1^n)^2 - \frac{2V_2^n}{\Delta x}}}$ respectively.

In (19) and (20), we substitute for $\tilde{H}_{1,2}^{n+1}$ from (22) and rearrange implicit and explicit terms. Due to the properties of the matrix \mathbf{A} , the terms $(\mathbf{R}^* \Delta \mathbf{R}_1)^T \mathbf{A}^{-1} (\Theta^* \Delta \mathbf{R})$, $(\mathbf{R}^* \Delta \mathbf{R}_1)^T \mathbf{A}^{-1} \Delta \mathbf{R}$, $(\mathbf{R}^* \Delta \mathbf{R}_2)^T \mathbf{A}^{-1} (\Theta^* \Delta \mathbf{R})$, and $(\mathbf{R}^* \Delta \mathbf{R}_2)^T \mathbf{A}^{-1} \Delta \mathbf{R}$ are non-negative. Therefore, (19) and (20) constitute a nine-diagonal system of linear equations for $\tilde{V}_{1,2}^{n+1}$, which is schematically drawn for a general configuration with dry regions in Fig. 3. The system is strictly diagonally dominant, generally non-symmetric due to the coupling bands and can be solved by biconjugate gradient (stabilized) method [32].

Before solving (15) for axial velocities $\tilde{\mathbf{U}}_{i+1/2}^{n+1}$, it is recommended to replace $\tilde{H}_{1,2}^{n+1}$ with $\tilde{V}_{1,2}^{n+1}$ using (22) in order to maintain mass conservation. After having determined preliminary fields \tilde{u} , \tilde{w} , and $\tilde{V}_{1,2}$, the predictor step is finished and we may proceed to the corrector step.

3.2. Corrector step

After the predictor step, it is necessary to calculate hydrodynamic pressure q in a way that the continuity equation (3) is fulfilled. New fields u , w , and $V_{1,2}$ are found by correcting the preliminary fields \tilde{u} , \tilde{w} , and $\tilde{V}_{1,2}$ using the continuity equation given by (3) and the following fractional step equations

$$u_{i+1/2,j}^{n+1} = \tilde{u}_{i+1/2,j}^{n+1} - \theta \frac{\Delta t}{\Delta x} (q_{i+1,j}^{n+1} - q_{i,j}^{n+1}) \tag{23}$$

$$w_{i,j+1/2}^{n+1} = \tilde{w}_{i,j+1/2}^{n+1} - \theta \frac{\Delta t}{\Delta x} (q_{i,j+1}^{n+1} - q_{i,j}^{n+1}) \tag{24}$$

In each bulk cell i.e. a cell other than that at the free-surface, the discretized form of the continuity equation can be expressed by

$$u_{i+1/2,j}^{n+1} r_{i+1/2,j}^n \Delta r_{i+1/2,j}^n - u_{i-1/2,j}^{n+1} r_{i-1/2,j}^n \Delta r_{i-1/2,j}^n + w_{i,j+1/2}^{n+1} r_{i,j+1/2}^n \Delta x - w_{i,j-1/2}^{n+1} r_{i,j-1/2}^n \Delta x = 0 \tag{25}$$

At the free-surface, the incompressibility condition can be written as

$$(V_1 + V_2)_i^{n+1} = (V_1 + V_2)_i^n + \theta \Delta t w_{i,N-1/2}^{n+1} r_{i,N-1/2}^n \Delta x - \theta \Delta t (u_{i+1/2,N}^{n+1} r_{i+1/2,N}^n \Delta r_{i+1/2,N}^n - u_{i-1/2,N}^{n+1} r_{i-1/2,N}^n \Delta r_{i-1/2,N}^n) \tag{26}$$

Assuming the pressure p being hydrostatic in the free-surface cells, the following condition applies

$$\Omega^2 R(r - R + H_1 + H_2) = \Omega^2 R(r - R + \tilde{H}_1 + \tilde{H}_2) + q \tag{27}$$

In order to be applied in (26), the hydrostatic condition (27) needs to be however reformulated in terms of replacing H with V at timestep $n + 1$. Using geometrical relations, (27) can be transformed into

$$V_1 + V_2 = \tilde{V}_1 + \tilde{V}_2 + \Delta x \left(R - \tilde{H}_1 - \tilde{H}_2 - \frac{q}{2\Omega^2 R} \right) \frac{q}{\Omega^2 R} \tag{28}$$

Similarly to (21), (28) is also non-linear and thus, a linearization is again applied to it. Then, $(V_1 + V_2)_i^{n+1}$ in (26) can be substituted with the linearized form of (28). Substituting (23)-(24) into (25) and (26), keeping terms with q on the lhs, and moving all other to the rhs, yields the system of Poisson’s equations approximated by finite differences. The properties of the system are dependent on the geometric configuration of the free-surface and the interface. When fluctuations of both, the free-surface and the interface, stay within two distinct radial layers or within a single radial layer of cells, the system of Poisson’s equations is diagonally dominant and symmetric. On the contrary, when the fluctuations of either of them become larger and spread over more than one radial layer of cells, the system is still diagonally dominant, no longer symmetric though. Both scenarios are depicted in Fig. 2. Concerning the scenario shown in Fig. 2b, the incompressibility condition for the highlighted free-surface cell takes slightly different form than (26), given by

$$(V_1 + V_2)_i^{n+1} = (V_1 + V_2)_i^n + \theta \Delta t w_{i,N-1/2}^{n+1} r_{i,N-1/2}^n \Delta x - \theta \Delta t \left(\sum_r u_{i+1/2,r}^{n+1} r_{i+1/2,r}^n \Delta r_{i+1/2,r}^n - \sum_s u_{i-1/2,s}^{n+1} r_{i-1/2,s}^n \Delta r_{i-1/2,s}^n \right), \tag{29}$$

where indices r, s are schematically explained in Fig. 2b. In Fig. 2b, the shaded cells are also considered as free-surface cells and therefore; the pressure p inside them is hydrostatic. This implies that the hydrodynamic pressure q is shared among all such free-surface cells at a given axial position $i + 1$. This approach greatly simplifies assembling of the system of Poisson’s equations as well as improves the convergence rate of finding the solution. A similar situation can be encountered at the interface, when its fluctuations surpass a single radial layer of cells (Fig. 2c). The incompressibility condition, given by (25), has to be modified and takes the following form

$$\sum_r u_{i+1/2,r}^{n+1} r_{i+1/2,r}^n \Delta r_{i+1/2,r}^n - \sum_s u_{i-1/2,s}^{n+1} r_{i-1/2,s}^n \Delta r_{i-1/2,s}^n + w_{i,M+1/2}^{n+1} r_{i,M+1/2}^n \Delta x - w_{i,M-1/2}^{n+1} r_{i,M-1/2}^n \Delta x = 0, \tag{30}$$

where r, s are again schematically explained in Fig. 2c. In addition, a similar assumption is applied to the hydrodynamic pressure q at pseudo-interface cells at a given axial position $i + 1$ such that it is constant.

Once the field of the hydrodynamic pressure q is determined, axial velocities u can be corrected using (23). In order to ensure divergence free velocity field, radial velocities w should be determined using the incompressibility condition rather than (24). By setting $w_{i,1/2}^{n+1}$ to zero, such condition can be written in the following form

$$w_{i,j+1/2}^{n+1} = \frac{1}{r_{i,j+1/2}^n \Delta x} \left(w_{i,j-1/2}^{n+1} r_{i,j-1/2}^n \Delta x - u_{i+1/2,j}^{n+1} r_{i+1/2,j}^n \Delta r_{i+1/2,j}^n + u_{i-1/2,j}^{n+1} r_{i-1/2,j}^n \Delta r_{i-1/2,j}^n \right) \tag{31}$$

Note that in free-surface cells and interface cells, the incompressibility condition may differ from (31). Finally, $V_{1,2}$ are recomputed using the following formulas

$$V_1^{n+1} = V_1^n - \Delta t \left(\sum_{j=1}^M r_{i+1/2,j}^n \Delta r_{i+1/2,j}^n u_{i+1/2,j}^{n+1} - \sum_{j=1}^M r_{i-1/2,j}^n \Delta r_{i-1/2,j}^n u_{i-1/2,j}^{n+1} \right) \tag{32}$$

$$V_2^{n+1} = V_2^n - \Delta t \left(\sum_{j=M+1}^N r_{i+1/2,j}^n \Delta r_{i+1/2,j}^n u_{i+1/2,j}^{n+1} - \sum_{j=M+1}^N r_{i-1/2,j}^n \Delta r_{i-1/2,j}^n u_{i-1/2,j}^{n+1} \right) \tag{33}$$

and the radial elements Δr are updated using the new values of $V_{1,2}$ from (32)-(33).

The heat advection–diffusion equation (4) is discretized in a finite volume framework as the following

$$\begin{aligned} & \rho_{i,j} c_{pi,j} (\Delta x r_{i,j}^{n+1} \Delta r_{i,j}^{n+1}) T_{i,j}^{n+1,m+1} + \Delta t \left[(\rho_{i,j+1/2} c_{pi,j+1/2} \Delta x r_{i,j+1/2}^n w_{i,j+1/2}^{n+1} T_{i,j+1/2}^{n+1,m+1} - \rho_{i,j-1/2} c_{pi,j-1/2} \Delta x r_{i,j-1/2}^n w_{i,j-1/2}^{n+1} T_{i,j-1/2}^{n+1,m+1}) \right. \\ & + (\rho_{i+1/2,j} c_{pi+1/2,j} r_{i+1/2,j}^n \Delta r_{i+1/2,j}^n u_{i+1/2,j}^{n+1} T_{i+1/2,j}^{n+1,m+1} - \rho_{i-1/2,j} c_{pi-1/2,j} r_{i-1/2,j}^n \Delta r_{i-1/2,j}^n u_{i-1/2,j}^{n+1} T_{i-1/2,j}^{n+1,m+1}) \\ & - \left(k_{i,j+1/2} \Delta x r_{i,j+1/2}^{n+1} \frac{T_{i,j+1}^{n+1,m+1} - T_{i,j}^{n+1,m+1}}{\Delta r_{i,j+1/2}^{n+1}} - k_{i,j-1/2} \Delta x r_{i,j-1/2}^{n+1} \frac{T_{i,j}^{n+1,m+1} - T_{i,j-1}^{n+1,m+1}}{\Delta r_{i,j-1/2}^{n+1}} \right) \\ & \left. - \left(k_{i+1/2,j} r_{i+1/2,j}^{n+1} \Delta r_{i+1/2,j}^{n+1} \frac{T_{i+1,j}^{n+1,m+1} - T_{i,j}^{n+1,m+1}}{\Delta x} - k_{i-1/2,j} r_{i-1/2,j}^{n+1} \Delta r_{i-1/2,j}^{n+1} \frac{T_{i,j}^{n+1,m+1} - T_{i-1,j}^{n+1,m+1}}{\Delta x} \right) \right] \\ & = \rho_{i,j} c_{pi,j} (\Delta x r_{i,j}^n \Delta r_{i,j}^n) T_{i,j}^n + S_{i,j}^{m+1} \end{aligned} \tag{34}$$

Both the thermal diffusion and the advection term are treated implicitly. At the cell faces, physical properties are determined using the upwind method, which naturally ensures the boundedness for the temperature field. The term, $S_{i,j}^{m+1}$, represents the latent heat source term due to solidification and, as explained later, a special scheme is required for $S_{i,j}^{m+1}$. Briefly, when the phase change takes place within a narrow range of temperatures denoted as the liquidus temperature and the solidus temperature, the source term is stiff and the algorithm should be able to prevent numerical oscillations of the solution, namely permanent switching between the liquid and the solid during two subsequent iterations. In order to achieve convergence between the temperature T and the liquid fraction g_i , (34) must be solved iteratively for a number of iterations, each denoted by the letter m . An appropriate discretization of $S_{i,j}^{m+1}$ may be of the following form [33]

$$S_{i,j}^{m+1} = -\rho_{i,j}L_f(\Delta x r_{i,j}^{n+1} \Delta r_{i,j}^{n+1}) \frac{dF}{dT} T_{i,j}^{n+1,m+1} + \rho_{i,j}L_f(\Delta x r_{i,j}^{n+1} \Delta r_{i,j}^{n+1}) \left[g_{i,i,j}^n - g_{i,i,j}^m + \frac{dF}{dT} F^{-1} \right], \tag{35}$$

where $\frac{dF}{dT}$ and F^{-1} are respectively the slope of the temperature dependent liquid fraction curve and the inverse of the liquid fraction g_i , both evaluated at $g_{i,i,j}^m$ from previous iteration. After solving (34) with $S_{i,j}^{m+1}$ given by (35), it is necessary to update the liquid fraction $g_{i,i,j}^{m+1}$ using the following formula

$$g_{i,j}^{m+1} = g_{i,j}^m + \frac{dF}{dT} (T_{i,j}^{n+1,m+1} - F^{-1}) \tag{36}$$

When the convergence is reached, $g_{i,j}^{m+1}$ is set equal to $g_{i,j}^{m+1}$ and we may proceed to the next time step.

Until here, the boundary conditions were not discussed except for those related to movement of the free-surface and the interface, known as the kinematic boundary conditions. Imposing other flow-related boundary conditions is quite straightforward. Along the normal direction to fixed walls, a zero flux is applied for both the velocity component and the hydrodynamic pressure. In addition, the tangential component of velocity is set zero there. Although not used in this study, discretization of the radial viscous term in the momentum equation for the axial component of velocity may be for example realized through the Manning–Chezy formula [34]. Similar formulas may be applied at the free-surface to mimic a stress resulting from a relative motion between the liquid layer and the surrounding gas. It is also possible to design an empirical formula for the viscous stress at the interface between the layers. In the present study namely in the numerical examples, viscous stresses are directly determined using the physical viscosity and dimensions of the finite-difference grid. At the free-surface, a zero stress is considered. In addition, the boundary conditions are also required for the heat-advection diffusion equation given by (4). Here, at the free-surface a Robin-type boundary condition is imposed to account for a convective heat transfer. At the walls, either a Neumann-type boundary condition or a coupled boundary condition is considered.

Concerning the properties of the method, it should be pointed out that by skipping the corrector step and setting the initial value of the hydrodynamic pressure $q_{i,j}^0$ to zero a hydrostatic velocity field is obtained. This feature of the method is beneficial in cases, when the type of flow is known in advance or can be estimated to be approximately hydrostatic. In such cases, computational costs drop significantly, as it is no longer necessary to solve the set of Poisson’s equations for the hydrodynamic pressure q , which is the most computationally expensive part of the algorithm.

The presented method can deal with two immiscible layers, from which the inner (top) layer must be lighter ($\rho_2 < \rho_1$) than the outer (bottom) layer. Opposite scenarios, when $\rho_2 \geq \rho_1$ and the Rayleigh–Taylor instability is expected to happen, cannot be however handled. Another important feature of the method is related to the layer depths $H_{1,2}$ extending only over a single layer of cells along the radial direction. The algorithm conveniently transforms into the shallow water equations, often used in oceanography and meteorology e.g. in modeling of geostrophic flows.

When it comes to implicit coupling of the free-surface/interface position and the velocity field, the method turns out to be unconditionally stable for $1/2 \leq \theta \leq 1$. Therefore, the time step is independent of the free-surface/interface wave speeds and radial viscosity terms. Due to explicit treatment of the axial viscosity terms, a time step restriction however exists and is given by [35].

$$\Delta t \leq \Delta x^2 / (4\nu) \tag{37}$$

As long as the axial grid size Δx stays much larger, the time step restriction (37) stays rather weak. Currently, there appears to be a second restriction of the time step related to the radial velocity w , namely the radial velocity of the free-surface and the interface, and solving the heat advection–diffusion equation (34). As the algorithm requires both the free-surface and the interface not to cross more than one layer of cells in radial direction, the following convective limit CFL applies

$$\Delta t^{n+1} \leq \min \left(\frac{\Delta r}{H_1^{n+1} - H_1^n}, \frac{\Delta r}{H_1^{n+1} + H_2^{n+1} - H_1^n - H_2^n} \right) \tag{38}$$

where Δr is the radial size of the background grid cell rather than the radial size of the actual element. The last stability limit (38) could be possibly removed by splitting the time step Δt into a number of equal-size substeps and use a subcycling when solving (34).

4. Numerical examples and discussion of results

This section demonstrates the capabilities of the proposed method on several numerical examples. Some examples are compared with results of other numerical techniques and some are verified against experimental data.

4.1. Example 1: single-layer hydrostatic vs. full model

The first example is intended to show that when the ratio of radial and axial characteristic scales is small ($\ll 1$), the flow is nearly hydrostatic. Therefore, it is possible to omit the hydrodynamic pressure q from the momentum equations. In the present method it is realized by setting the initial value $q_{i,j}^0$ to zero and skipping the corrector step. Here, two different single-layer cases (a) and (b) are considered with a short and a long wave initial disturbance of the free-surface respectively, given by the following formulas

$$\begin{aligned} (a) : H_1^0(x) &= 0.06 + \max(0.02 - 5(x - 0.5)^2, 0) \\ (b) : H_1^0(x) &= 0.06 + \max(0.02 - 5(x - 5)^2, 0) \end{aligned} \quad (39)$$

In addition to the free-surface, fixed walls with no-slip condition are bounding the finite-volume grid with 100×100 cells. Physical properties such as the density and the dynamic viscosity are set to 7700 kgm^{-3} and 0.006 Pas respectively. The size of the time step Δt is adjusted during the calculation in order to maintain $CFL = 0.95$. The implicitness factor θ is set to 0.55 . At $t = 0 \text{ s}$, the free-surface is described by (39). Later, due to the g-force ($100g$) the parabolic disturbance collapses and waves propagate toward the left and the right wall. The g-force is a term often used by centrifugal casting community to express the centrifugal acceleration $\Omega^2 R$ as a multiple of the gravitational acceleration g . The g-force of $100g$ is a typical value encountered during the centrifugal casting. In Fig. 4a and b, the scenarios are depicted respectively for the case (a) and (b). The contours represent a distribution of the hydrodynamic pressure q . While the hydrostatic assumption is obviously justified in the case (a), in the case (b) such assumption is clearly incorrect, meaning that the hydrodynamic pressure has to be accounted for. As a result, the hydrostatic model, greatly saving the computational resources, should only be used, when the ratio of radial and axial characteristic scales $\ll 1$. Otherwise, it is necessary to consider the full model with the hydrodynamic pressure included.

4.2. Example 2: two-layer hydrostatic model vs. shallow water equations

Here, a test case with two layers is suggested with initial conditions shown in Fig. 5. Gradients of the hydrostatic pressure again serve as a driving force for a fluid motion and also provide a momentum coupling between the layers. The coupling is also realized through a viscous stress term. A simulation work was performed using the hydrostatic model, followed by the numerical verification conducted with the help of the radially averaged shallow water equations solved using the approximate Riemann solver with high resolution corrections [36] developed earlier by the authors [37]. Initially, the bottom layer is flat, whereas the top layer is disturbed with a parabolic hump. Initial conditions are patched on the domain using the following formulas

$$\begin{aligned} \text{the bottom layer : } H_1^0(x) &= 0.045 \\ \text{the top layer : } H_2^0(x) &= 0.015 + \max(0.03 - 500(x - 0.05)^2, 0) \end{aligned} \quad (40)$$

The densities, ρ_1 and ρ_2 , are set to 7700 kgm^{-3} and 7600 kgm^{-3} respectively. The dynamic viscosities are identical, equal to 0.006 Pas . In Fig. 5, it is shown that both techniques produce almost identical results at $t = 0 \text{ s}$. Later, the deviations will certainly grow. The reader should be reminded that it is difficult to say, which algorithm is more accurate namely for the following reasons. Unlike the hydrostatic model discretized on a two-dimensional finite-volume grid, the SWE model requires only one (axial) space dimension. On the other hand, the approximate Riemann solver physically correctly decomposes the hyperbolic PDEs into a set of discontinuities moving with certain wave speeds. The solution is found using TVD updating formulas with limiters, unwinding each discontinuity separately. One significant drawback of the two-layer approximate Riemann solver for the SWE is a way of determining the wave speeds, namely the one representing the momentum transfer between the layers. It was shown that when ρ_2 is significantly smaller than ρ_1 , than such a wave speed is not correctly approximated [38]. In Fig. 5, the layer densities are quite similar and both methods deliver almost identical results. In Fig. 6, $\rho_2 \ll \rho_1$ such that $\rho_1 = 7700 \text{ kgm}^{-3}$ and $\rho_2 = 1000 \text{ kgm}^{-3}$, the results are hardly comparable due to the erroneous wave speed approximation in the SWE model. Only the hydrostatic model thus gives a physically reasonable propagation of waves (solid lines in Fig. 6).

4.3. Example 3: thermal convection

This example shows two cases with the thermal convection. In both cases, the free-surface is initially disturbed by the following function

$$H_1^0(x) = 0.03 + 0.005 \sin(2\pi x/L) \quad (41)$$

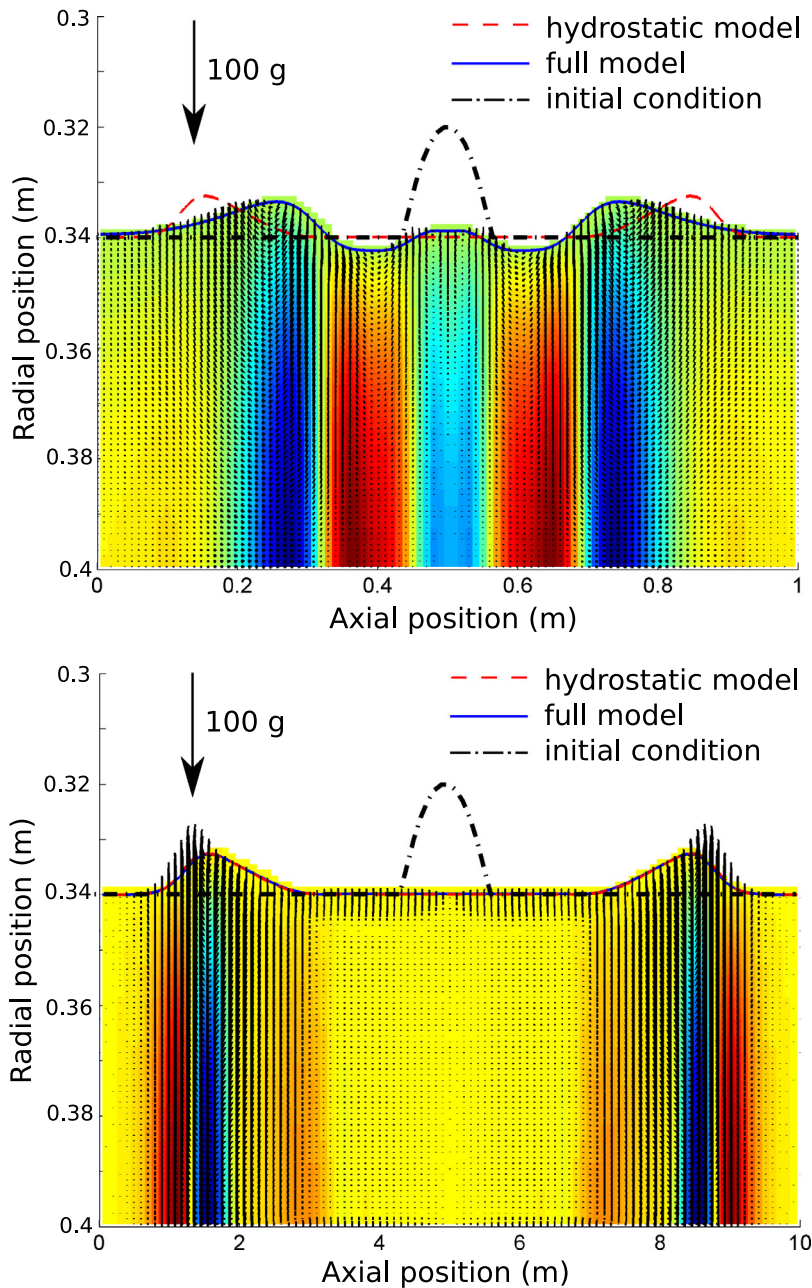


Fig. 4. An initial parabolic perturbation of the free-surface producing waves propagating to the left and to the right; (a) a short wave case $t = 0.125$ s; (b) a long wave case (\sim hydrostatic) at $t = 1.25$ s.

where $L(L = 0.1\text{m})$ denotes the axial dimension of the computational domain. In the first case, the thermal convection is induced by cooling applied at the free-surface, numerically represented by a constant heat transfer coefficient htc . Remaining boundaries are treated as adiabatic walls. The characteristic time of the free-surface motion is set close to that of the thermal convection, so that both phenomena can be observed at the same time. Material properties and other parameters are listed in Table 1. As the time proceeds, due to the cooling the liquid close to the free-surface becomes heavier and starts sinking toward the bottom. The instability, also known as the Rayleigh-Bénard instability, is triggered by oscillations of the free-surface. Eventually, the gravity waves, dictating the actual shape of the free-surface, are taken over by the thermal convection in this case. In Fig. 7, thermal convection patterns interacting with the free-surface are shown at time $t = 1$ s.

In the second case, the cooling of the same intensity htc is applied at the bottom, while the cooling at the free-surface is stopped. In order to promote rising plumes of the colder liquid within the bulk of the hot liquid, the sign of the

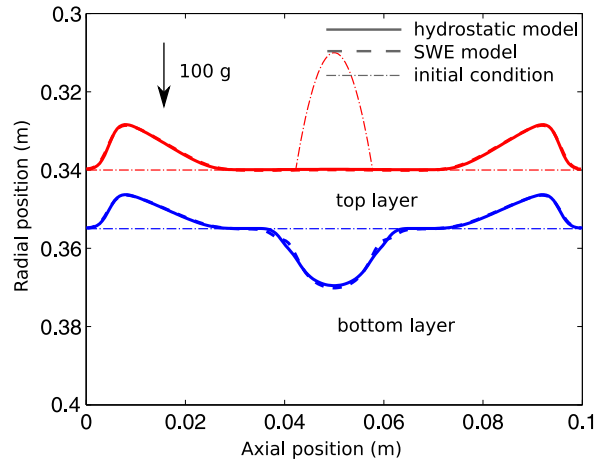


Fig. 5. The present numerical model vs. the approximate Riemann solver for the shallow water equations with two layers of similar densities ($\rho_1 = 7700 \text{ kgm}^{-3}$, $\rho_2 = 7600 \text{ kgm}^{-3}$) at $t = 0.014 \text{ s}$.

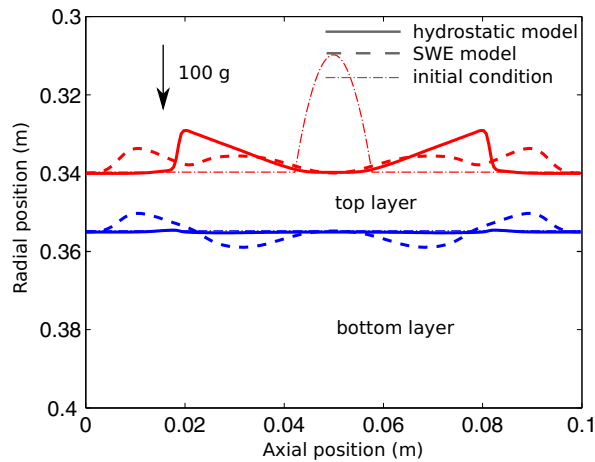


Fig. 6. The present numerical model vs. the approximate Riemann solver for the shallow water equations with two layers of significantly different densities ($\rho_1 = 7700 \text{ kgm}^{-3}$, $\rho_2 = 1000 \text{ kgm}^{-3}$) at $t = 0.014 \text{ s}$.

Table 1
Physical properties and parameters used in Example 3.

Property/parameter name	Symbol	Value	Unit
Grid	$N_x \times N_y$	100 × 100	–
Convective time step limit	CFL	0.95	–
Implicitness factor	θ	0.55	–
Gravitational acceleration	g	10	m s^{-2}
Density	ρ	7700	kg m^{-3}
Dynamic viscosity	μ	0.006	Pa s
Thermal conductivity	k	20	$\text{W m}^{-1} \text{K}^{-1}$
Specific heat	c_p	500	$\text{J kg}^{-1} \text{K}^{-1}$
Heat transfer coefficient	htc	10	$\text{kW m}^{-2} \text{K}^{-1}$
Ambient temperature	T_a	2.5	$^\circ\text{C}$
Reference temperature	T_{ref}	1450	$^\circ\text{C}$
Thermal expansion coefficient	β	0.001	K^{-1}

thermal expansion coefficient β has to be switched so that the colder liquid becomes lighter ($\beta \rightarrow -\beta$). Other material properties and parameters are identical to those summarized in Table 1. In Fig. 8, again a snapshot of the temperature field reflecting the thermal convection is presented at time $t = 1 \text{ s}$. In addition, the position of the free-surface is also plotted at $t = 0.25 \text{ s}$. The dashed lines indicate the position of the free-surface calculated using the volume of fluid model available in ANSYS FLUENT 14.5 with the properties and parameters given in Table 1. Note that here β is referred to as a thermal

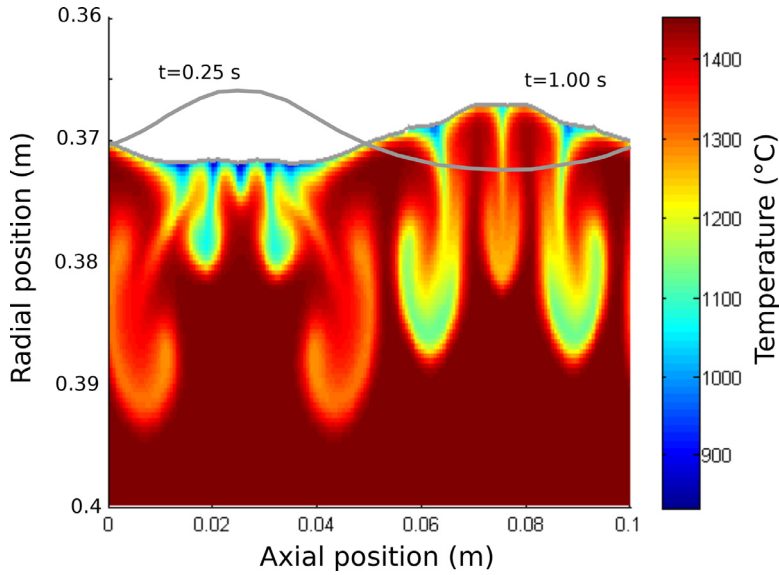


Fig. 7. An example of a thermal convection induced by the cooling applied at the free-surface, initially disturbed by (41), at $t = 1$ s.

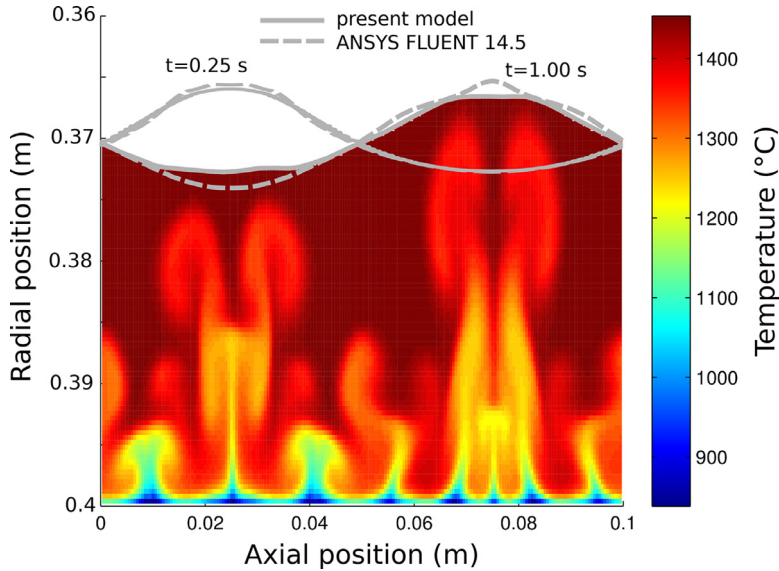


Fig. 8. Thermal convection at $t = 1$ s induced by the cooling applied at the bottom wall. A free-surface calculated by the present numerical model (solid line) compared to that obtained using ANSYS FLUENT 14.5 (dashed line).

expansion coefficient. It could however also represent a solutal expansion coefficient. In that case the corresponding advection-diffusion equation would be solved for the concentration and not for the temperature.

4.4. Example 4: horizontal centrifugal casting (HCC)

A simulation of the HCC process, shortly described in Section 1, is presented here. The results are validated against in terms of comparing calculated and measured temperatures. A pyrometer and a thermo-camera were used to continuously record temperatures of a single point at the free-surface of the casting and the outer wall of the cylindrical mold respectively. The simulation was set up using a multi-region approach. The numerical model, detailed in the section Numerical algorithm, was employed only in the fluid region indicating the room for the casting. The solid regions such as the mold and both end cores were also discretized using finite-volume grids; however, only the heat diffusion equation was solved there for the temperature T with appropriate material properties and boundary conditions, which are due to confidentiality of industry data only roughly introduced in Table 2. The heat transport was solved simultaneously in all regions; therefore, there was no need for otherwise typical Neumann–Dirichlet coupling at the common walls.

Table 2
Physical properties and other parameters used in Example 4.

	symbol	value	Unit
Simulation settings			
Total number of cells	$N_x \times N_r$	~100k	–
Convective time step limit	CFL	0.95	–
Implicitness factor	θ	0.55	–
Thermal boundary conditions			
Free-surface	htc_{fs}	0	$W m^{-2} K^{-1}$
Mold and end core walls	$htc_{m,en}$	40	$W m^{-2} K^{-1}$
Ambient temperature	T_a	25	$^{\circ}C$
First layer			
Casting length	h	3	m
Layer thickness	H_1	0.1	m
Outer radius	R	0.4	m
Density	ρ	7600	$kg m^{-3}$
Dynamic viscosity	μ	0.006	Pa s
Thermal conductivity	k	22	$W m^{-1} K^{-1}$
Specific heat	c_p	600	$J kg^{-1} K^{-1}$
Reference temperature	T_{ref}	1450	$^{\circ}C$
Filling temperature	T_{fill}	1450	$^{\circ}C$
Thermal expansion coefficient	β	0.0001	K^{-1}
Latent heat	L_f	280	$kJ kg^{-1}$
Solidus temperature	T_s	1165	$^{\circ}C$
Liquidus temperature	T_l	1322	$^{\circ}C$
Liquid fraction	–	Linear	–
Second layer			
Layer thickness	H_2	0.15	m
Density	ρ	7200	$kg m^{-3}$
Dynamic viscosity	μ	0.006	Pa s
Thermal conductivity	k	25	$W m^{-1} K^{-1}$
Specific heat	c_p	450	$J kg^{-1} K^{-1}$
Reference temperature	T_{ref}	1450	$^{\circ}C$
Filling temperature	T_{fill}	1420	$^{\circ}C$
Thermal expansion coefficient	β	0.0001	K^{-1}
Latent heat	L_f	200	$kJ kg^{-1}$
Solidus temperature	T_s	1080	$^{\circ}C$
Liquidus temperature	T_l	1250	$^{\circ}C$
Liquid fraction	–	Linear	–
Mold			
Rotation rate	Ω	70	$rad s^{-1}$
Mold thickness	mt	0.2	m
Density	ρ	7850	$kg m^{-3}$
Thermal conductivity	k	60	$W m^{-1} K^{-1}$
Specific heat	c_p	490	$J kg^{-1} K^{-1}$
End cores			
Density	ρ	2200	$kg m^{-3}$
Thermal conductivity	k	10	$W m^{-1} K^{-1}$
Specific heat	c_p	200	$J kg^{-1} K^{-1}$
Coating			
Thermal conductivity	k	5	$W m^{-1} K^{-1}$
Coating thickness	ct	0.004	m

A layout of the computational domain is obvious from looking at Fig. 9, with the mold at the top, the end cores at both sides, and the casting region in the center. In addition, temperature contours are shown inside both layers at $v t \approx 35$ min along with isolines of liquid fraction, namely $g_l = 0.01$ (solid line) and $g_l = 0.99$ (dash line). The marker at the free-surface denotes the target point of a single channel IR thermometer, at which the temperature was recorded with frequency of 100 Hz. The IR thermometer (Infratherm ISQ 5) was calibrated to a single temperature of $\sim 1450^{\circ}C$ and it was mounted at a fixed position schematically shown in Fig. 9. In Fig. 10, the calculated cooling curve (thick solid line) quite reasonably follows IR thermometer curve (thin solid line) obtained by averaging temperature records from several castings of the same product. The error bars corresponds to relative errors of $\pm 5\%$. The sudden jump of the temperature at $t = 33$ min is caused by pouring the second layer. During the pouring, the IR thermometer measurement was interrupted; data is therefore not available. The experimental data is also missing at the early stage of the casting namely during the pouring of the first layer. In addition to IR thermometer measurements, a thermal camera (FLIR ThermoCAM 540; frequency 0.1 Hz) was employed to monitor temperatures of the entire surface of the mold visible from outside (Fig. 11). For comparison with the numerical results, only a single value of temperature was however used, obtained by averaging temperature field along the black solid line shown in Fig. 11. Looking at the evolution of the average temperature of the outer mold surface in Fig. 10, it can be concluded that the calculated and the measured data are in a good agreement. Relative errors

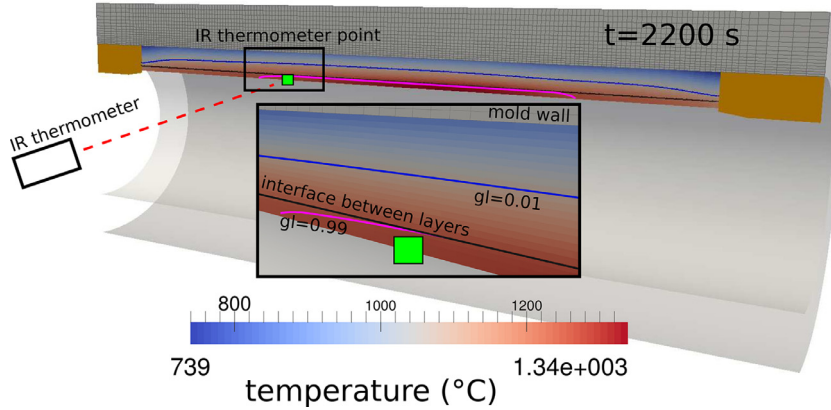


Fig. 9. Results of horizontal centrifugal casting simulation namely temperature contours and isolines of the liquid fraction $g_l = 0.01$ (solid line) and $g_l = 0.99$ (dashed line) demarcating the mushy zone at $t = 35$ min. The circle marker denotes the target point of the pyrometer. In addition to the casting region, the mold and two end cores are visible.

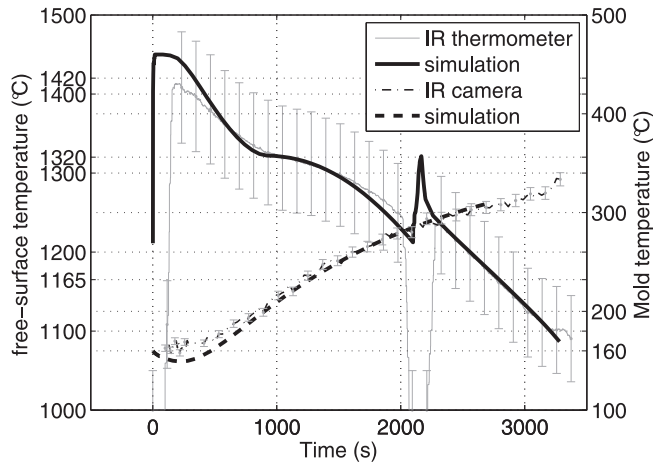


Fig. 10. Cooling curves calculated using the present numerical model plotted against those obtained from the pyrometer and thermo-camera measurements.

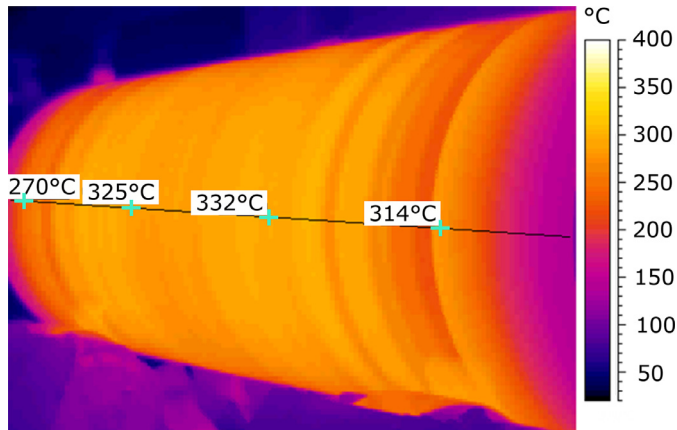


Fig. 11. Thermal camera image taken at around 35min.

of thermal camera measurements are expected to fall into a typical range $\pm 2\%$ [39]. Although the numerical results were successfully compared against two different kinds of temperature measurement techniques, further verifications are still required mainly for the following reasons. Excellent match of temperatures of the outer surface of the mold cannot be considered as a conclusive and sufficient verification, as it is located far from the casting and at the same time it is very much influenced by the accuracy of the thermal boundary condition imposed there. Concerning IR thermometer measurements, these were performed exclusively at a single location at the free-surface. The reader should be reminded of two things. Firstly, the flow was solved in $x - r$ plane and thus some features, peculiarities caused by the Coriolis force may have been missed. Secondly, in this study the solutal transport was not taken into account. However, during the real casting the solutal convection will be quite pronounced especially due to significant centrifugal forces, providing a good mixing in the liquid.

5. Conclusions

A semi-implicit finite-difference/volume-based model has been proposed to numerically investigate a free-surface flow of a single or two immiscible liquid layers, with a special focus on the horizontal centrifugal casting process. The numerical model is based on valuable and comprehensively processed works done by Casulli [23–25]. Here, the governing equations and the numerical algorithm were derived in the cylindrical coordinate system in two space dimensions, namely the axial and the radial coordinates. Switching to the Cartesian coordinate system is straightforward and in fact, it eventually results in a simpler algorithm, as all the linearization steps described earlier in section Numerical algorithm drop out. The main idea of the algorithm is to split the pressure term into the hydrostatic pressure and the hydrodynamic pressure. The algorithm is divided into two steps, the predictor step and the corrector step. The pressure is discretized by the θ -method, allowing the user to set the level of its implicitness. Both explicit and implicit contributions of the hydrostatic pressure are included in the predictor step. While the explicit part of the hydrodynamic pressure is applied there also, the implicit part is determined separately in the corrector step. The convective term, the axial viscous terms, the gradient of the baroclinic pressure are discretized explicitly in the predictor step. Preliminary fields of the layer depths and velocity obtained in the predictor step are subsequently updated in the corrector step. In addition to the flow, the heat advection-diffusion equation is solved in a fractional step. When the solidification is taken into account through the latent heat source term, generally several iterations (~ 3) are needed to reach a convergence between the liquid fraction g_l and the temperature T . Concerning the stability, due to the implicit discretization of the gradient of the hydrostatic pressure the proposed algorithm is unconditionally stable with respect to the free-surface/interface wave speed. Yet a certain restriction on the time step exists due to the explicit discretization of the axial viscous terms. As long as the axial grid spacing is large compared to the radial one, such a time step restriction is rather weak. In addition, the time step is restricted also by the convective limit (CFL) arising when solving the heat advection-diffusion equation. In that case, the free-surface or the interface should not cross more than one computational cell in the radial direction within a single time step ($CFL < 1$).

As shown in the numerical examples, the algorithm can be easily modified into a hydrostatic model by setting the initial value of the hydrodynamic pressure to zero and skipping the corrector step. It was also mentioned that when the liquid layer(s) fits into a single layer of radial computational cells, the algorithm naturally converts into a solver for the single or the two-layer shallow water equations. The algorithm has been successfully validated against the experimental data obtained during the horizontal centrifugal casting process.

Acknowledgments

Financial support by the Austrian Federal Government (in particular from the Bundesministerium fuer Verkehr, Innovation und Technologie and the Bundesministerium fuer Wirtschaft, Familie und Jugend) and the Styrian Provincial Government, represented by Oesterreichische Forschungsforderungsgesellschaft mbH and by Steirische Wirtschaftsforderungsgesellschaft mbH, within the research activities of the K2 Competence Centre on "Integrated Research in Materials, Processing and Product Engineering", operated by the Materials Center Leoben Forschung GmbH in the framework of the Austrian COMET Competence Centre Programme, is gratefully acknowledged. This work is also financially supported by the Eisenwerk Sulzau-Werfen R. & E. Weinberger AG.

References

- [1] A. Coutinho, Some reflections on big data and computational mechanics, *IACM Expressions* 35 (2014) 5–7.
- [2] S. Elgeti, H. Sauerland, Deforming fluid domains within the finite element method: five mesh-based tracking methods in comparison, *Arch. Comput. Method Eng.* 23 (2) (2015) 1–39.
- [3] S. Osher, J.A. Sethian, Fronts propagating with curvature-dependent speed: algorithms based on Hamilton–Jacobi formulations, *J. Comput. Phys.* 79 (1988) 12–49.
- [4] J.A. Sethian, *Level set methods and fast marching methods: evolving interfaces in computational geometry*, Fluid Mechanics, Computer Vision, and Materials Science, Cambridge University Press, 1999 ISBN 0-521-64557-3.
- [5] H.C.W. Hirt, B.D. Nichols, Volume of fluid (VOF) method for the dynamics of free boundaries, *J. Comput. Phys.* 39 (1) (1981) 201–225.
- [6] W.J. Boettinger, J.A. Warren, C. Beckermann, A. Karma, Phase-field simulation of solidification, *Annu. Rev. Mater. Res.* 32 (2002) 163.
- [7] R. Folch, J. Casademunt, A. Hernández-Machado, L. Ramírez-Piscina, Phase-field model for Hele-Shaw flows with arbitrary viscosity contrast. II. Numerical study, *Phys. Rev. E* 60 (2) (1999) 1734.
- [8] F.H. Harlow, J.E. Welch, Numerical calculation of time-dependent viscous incompressible flow of fluid with a free surface, *Phys. Fluids* 8 (1965) 2182–2189.

- [9] J.H. Ferziger, M. Perić, *Computational Methods for Fluid Dynamics*, vol. 3, Springer, Berlin, 2002.
- [10] T.E. Tezduyar, Interface-tracking, interface-capturing and enhanced solution techniques, *Mecanica Comput.* 21 (2002) 116–135.
- [11] T. Bjontegaard, E.M. Ronquist, Accurate interface-tracking for arbitrary, Lagrangian-Eulerian Schemes 228 (12) (2009) 4379–4399.
- [12] R.J. Leveque, *Finite Volume Methods For Hyperbolic Problems*, Cambridge University Press, 2002, p. 429.
- [13] D. George, *Finite volume Methods and adaptive refinement for tsunami propagation and inundation* Ph.D. thesis, University of Washington, 2006, p. 6.
- [14] J. Bohacek, A. Kharicha, A. Ludwig, M. Wu, Simulation of horizontal centrifugal casting: mold filling and solidification, *ISIJ Int.* 54 (2) (2014) 266–274.
- [15] J. Bohacek, A. Kharicha, A. Ludwig, M. Wu, Shallow water model for horizontal centrifugal casting, *IOP Conf. Ser.: Mater. Sci. Eng.* 33 (2012) 012032.
- [16] E. Kaschnitz, Numerical simulation of centrifugal casting of pipes, *IOP Conf. Ser.: Mater. Sci. Eng.* 33 (2012) 012031.
- [17] H. Esaka, K. Kawai, H. Kaneko, K. Shinozuka, In-situ observation of horizontal centrifugal casting using a high-speed camera, *IOP Conf. Ser.: Mater. Sci. Eng.* 33 (2012) 012041.
- [18] L. Nastac, Numerical modeling of carbide redistribution during centrifugal casting of HSS shell rolls, *ISIJ Int.* 54 (6) (2014) 1294–1303.
- [19] S. Vacca, M.A. Martorano, R. Heringer, M. Bocallini, Determination of the heat transfer coefficient at the metal-mold interface during centrifugal casting, *Metall. Mater. Trans. A* 46A (2015) 2238–2248.
- [20] K.S. Keerthi Prasad, M.S. Murali, P.G. Mukunda, Analysis of fluid flow in centrifugal casting, *Front. Mater. Sci. China* 4 (1) (2010) 103–110.
- [21] D. McBride, N. Humphreys, T. Croft, N. Green, M. Cross, P. Withey, Complex free surface flows in centrifugal casting: computational modelling and validation experiments, *Comput. Fluids* 82 (2013) 63–72.
- [22] Z. Xu, N. Song, R.V. Tol, Y. Luan, D. Li, Modelling of horizontal centrifugal casting of work roll, *IOP Conf. Ser.: Mater. Sci. Eng.* 33 (2012) 012003.
- [23] V. Casulli, P. Zanolli, Semi-implicit numerical modeling of nonhydrostatic free-surface flows for environmental problems, *Math. Comput. Modell.* 36 (2002) 1131–1149.
- [24] V. Casulli, A semi-implicit finite difference method for non-hydrostatic, free-surface flows, *Int. J. Numer. Methods Fluids* 30 (1999) 425–440.
- [25] V. Casulli, A semi-implicit numerical method for the free-surface Navier–Stokes equations, *Int. J. Numer. Methods Fluids* 74 (8) (2014) 605–622.
- [26] A. Staniforth, A. White, N. Wood, Analysis of semi-Lagrangian trajectory computations, *Q. J. R. Meteorol. Soc.* 129 (591) (2003) 2065–2085.
- [27] I.G. Gospodinov, V.G. Spiridonov, J.-F. Geleyn, Second-order accuracy of two-time-level semi-Lagrangian schemes, *Q. J. R. Meteorol. Soc.* 127 (573) (2001) 1017–1033.
- [28] J.P. Gu, C. Beckermann, Simulation of convection and macrosegregation in a large steel ingot, *Metall. Mater. Trans. A* 30A (1999) 1357–1366.
- [29] M. Wu, A. Vakhrusev, G. Nunner, C. Pfeiler, A. Kharicha, A. Ludwig, Importance of melt flow in solidifying mushy zone, *Open Transp. Phenom. J.* 2 (2010) 16–23.
- [30] S. Vitousek, O.B. Fringer, Stability and consistency of nonhydrostatic free-surface models using semi-implicit θ -method, *Int. J. Numer. Methods Fluids* 72 (2013) 550–582.
- [31] M.R. Hestenes, E. Stiefel, Methods of conjugate gradients for solving linear systems, *J. Nat. Bur. Stand.* 49 (6) (1952) 409–436.
- [32] H.A. Van der Vorst, Bi-CGSTAB: a fast and smoothly converging variant of Bi-CG for the solution of nonsymmetric linear systems, *SIAM J. Sci. Stat. Comput.* 13 (2) (1992) 631–644.
- [33] V.R. Voller, C.R. Swaminathan, General source-based method for solidification phase change, *Numer. Heat Transfer B* 19 (1991) 175–189.
- [34] J. Murillo, P. Garcia-Navarro, Wave Riemann description of friction terms in unsteady shallow flows: Application to water and mud/debris floods, *J. Comput. Phys.* 231 (2012) 1963–2001.
- [35] H. Johnston, J.-G. Liu, Accurate, stable and efficient Navier-Stokes solvers based on explicit treatment of the pressure term, *J. Comput. Phys.* 199 (2004) 221–259.
- [36] B. Van Leer, Towards the ultimate conservative difference scheme III. Upstream-centered finite-difference schemes for ideal compressible flow, *J. Comput. Phys.* 23 (3) (1977) 263–275.
- [37] J. Bohacek, A. Kharicha, A. Ludwig, M. Wu, A. Paar, M. Brandner, L. Elizondo, T. Trickl, An approximate Riemann solver for two layer shallow water equations in horizontal centrifugal casting, in: *6th Int. Conf. Modelling and Simulation of Metall. Processes in Steelmaking*, 2015, pp. 1–8.
- [38] K.T. Mandli, *Finite volume methods for the multilayer shallow water equations with applications to storm surges* Ph.D. thesis, University of Washington, 2011, p. 52.
- [39] K. Pacholski, B. Wiecek, Practical assessment of accuracy of thermographic indirect measurements, *Meas. Autom. Monit.* 61 (2015) 278–281.